Synthesis and Characterization of BaCe0.4Zr0.4Pr0.2O3−δ Mixed Conductor Perovskite

Juan Basbus (juanbasbus@hotmail.com)
Centro Atomico Bariloche

M. Arce
Centro Atomico Bariloche

F. Prado
CONICET Bahia Blanca

H. Troiani
Centro Atomico Bariloche

A. Serquis
Centro Atomico Bariloche

L. Mogni
Centro Atomico Bariloche

Research Article

Keywords: BaCe0.4Zr0.4Pr0.2O3−δ (BCZP) perovskite, crystallographic, microstructural and thermodynamic study, electrochemical characterization, carbonation resistance, composite, buffer material, gas separation co-ionic membranes

Posted Date: July 2nd, 2020

DOI: https://doi.org/10.21203/rs.3.rs-37872/v1

Abstract

Compounds based on barium cerates and zirconates $Ba(Ce,Zr)O_{3-\delta}$ are oxides able to transport protons through their crystal lattice by proton hopping between oxygen sites. This feature makes them potential candidates as hydrogen sensors, membranes for hydrogen purification and isotopic exchange, and electrolyte for Proton Conducting Solid Oxide Fuel Cell (PC-SOFC) and Solid Oxide Electrolyzer Cells (PC-SOEC). Pr-doping on these family compounds decreases sintering temperature and introduces electronic conductivity. This work presents a systematic study of the high temperature properties of the $BaCe_{0.4}Zr_{0.4}Pr_{0.2}O_{3-\delta}$ (BCZP) perovskite in view of its potential use for these applications. At room temperature, BCZP presents rhombohedral structure, which transforms reversibly to cubic at 550 °C in dry air. Electrochemical measurements under dry air, wet air with water vapor (~ 2% H_2O) and heavy water vapor (~ 2% D_2O) were employed to describe bulk ionic and electronic transport above 200 °C. The total conductivity data exhibit behavior changes between 400 and 600 °C which could be associated to a crystal structure transition. Below 600 ºC BCZP presents low total conductivity, which limits its applications as single phase cathode material for electrochemical applications. However, the material has good thermomechanical compatibility with electrolytes (~ 11×10^{-6} K^{-1}) and high CO_2 tolerance (T > 900 ºC). These properties suggest that this compound could be used as oxide support for composite or impregnated electrodes, buffer layer to improve the performance of another cathode material or gas separation co-ionic membranes.

Highlights

The incorporation of a small amounts of water below 300 °C was confirmed.

BCZP presents a 2nd order phase transition between 400 and 600 ºC.

The total conductivity was essentially independent of water content on O_2-atmosphere and no hydrogen/deuterium isotopic effect was observed.

BCZP presents TECs compatible with typical electrolytes and high CO_2 resistance.

This material could be used as a constituent of a composite and/or buffer layer for PC-SOFC or gas separation co-ionic membranes.

Introduction

Proton conducting oxides are interesting materials for economic and sustainable energy conversion and storage devices such as protonic ceramic fuel cells, protonic ceramic electrolysis cells, gas purification and separation membranes, syn-gas membrane, ammonia synthesis, etc. [1–4].

Solid Oxide Fuel Cells (SOFC) are electrochemical devices based on oxides that transform the chemical energy from hydrogen or other fuels into electricity and heat. Proton conductor SOFC (PC-SOFC) have the

particularity that electrolytes exhibit protonic conduction. These devices presents high efficiency, low environmental impact, operating temperatures between 400 and 800 ºC, good stability and durability [5–8]. The search for new materials for PC-SOFC is a major topic in materials research. In the case of electrodes, different synthesis routes and compositions have been studied to obtain porous materials with small particle sizes and high purity, to ensure a high active surface area, i.e. low polarization resistance and power density increase [9, 10]. Several compositions were proposed as PC-SOFC cathodes: $BaCe_{0.4}Sm_{0.2}Fe_{0.4}O_{3-\delta}$ [11], $NdBaCo_2O_{5+\delta}$ [12], $Ba_{0.5}Sr_{0.5}Fe_{0.8}Cu_{0.2}O_{3-\delta}$ [13, 14], $Sm_{0.5}Sr_{0.5}Fe_{0.8}Cu_{0.2}O_{3-\delta}$ [15, 16], etc. They were tested as single cells, reaching power density values between 150 and 500 $mWcm^{-2}$ in the temperature range of 600 to 700 ºC. In addition, mixed proton-ionic and electronic conductors as well as co-H^+/O^{-2} ionic conductors are proposed for technological applications, such as gas separation membrane reactors in non-oxidative dehydrogenation processes [17–19] or high temperature humidity sensors [20].

On the other hand, it was reported that the incorporation of Pr in barium cerates and zirconates decreases sintering temperatures, improves the mechanical properties, increases CO_2 tolerance and introduces Mixed Ionic Electronic Conductivity (MIEC) [21–27]. To the best of our knowledge, there is no study on the high temperature properties of $BaCe_{0.4}Zr_{0.4}Pr_{0.2}O_{3-\delta}$ (BCZP) perovskite.

In this work, we present the systematic characterization of BCZP at a wide temperature range for its electrochemical applications. This perovskite presents high carbonation resistance and thermomechanical compatibility with electrolytes. Even considering that the low total conductivity limits the use of BCZP as cathode, the compound presents interesting combined properties that makes it plausible for different electrochemical applications.

Experimental

$BaCe_{0.4}Zr_{0.4}Pr_{0.2}O_{3-\delta}$ (BCZP) perovskite was synthesized by Solid State Reaction (SSR) from stoichiometric amounts of high purity precursors $BaCO_3$ (99.98%), CeO_2 (99.9%), ZrO_2 (99%) and Pr_6O_{11} (99.9%) from Sigma-Aldrich company. The precursors were ball milled during 45 min at 500 rpm in an agate planetary ball mill, calcined at 1350 °C for 4 hours and sintered at 1600 °C during 12 hours. For both thermal treatments, powders were uniaxially pressed into pellets at 50 $kgcm^{-2}$ using a 10 mm matrix. In cases where powders were required, the dense pellets were grinded in mortar. The phase purity and crystallographic structure were evaluated by X-Ray diffraction (XRD), by using PANalytical Empyrean diffractometer with Bragg Brentano geometry, Cu K_α radiation, a graphite monochromator and a PIXcel^{3D} detector. Structural and microstructural parameters were obtained from the diffraction pattern by using the Rietveld method and the Fullprof Suite software [28]. The instrumental line broadening was obtained from XRD standard.

Microstructure of dense pellets was observed by Scanning Electron Microscopy (SEM) with a ZEISS Crossbeam 340 microscope. In addition, a powder sample was studied by Transmission Electron

Microscopy (TEM) by using a TECNAI F20 G2 FEI microscope. Both TEM and SEM microscopes are equipped with Energy Dispersive Spectroscopy (EDS) detectors for elementary analysis.

Crystal structure as a function of temperature was studied by XRD, between room temperature and 800 °C under dry 20% O_2/He atmosphere. The heating and cooling rates were 10 °Cmin^{-1} with dwell time of 10 min before measurements. Diffraction patterns at high temperatures were collected by using an Anton Paar HTK1200N furnace coupled to the PANalytical Empyrean diffractometer. Structural and experimental parameters at high temperatures were obtained by using sequential mode of the Fullprof Suite software [28].

The mass evolution of BCZP hydrated powder was studied by Thermogravimetry (TG), using a Cahn 1000 electrobalance [29]. Previously, the powder was annealed at 200 ºC under wet air during 4 hours. Reversibility of water incorporation into the structure was studied by thermal cycling from room temperature to 900 °C with a heating/cooling rate of 5 °Cmin^{-1} under atmospheric air. The thermal behavior for the same sample was analyzed by Differential Scanning Calorimetry (DSC) with a Modulated DSC 2910 TA Instruments at a heating/cooling rate of 5 °Cmin^{-1} between room temperature and 500 °C under air.

The density of fresh dense pellet of BCZP was measured by Archimedes method through hydrostatic weighing using the same electrobalance and diethyl phthalate as the immersion fluid [30, 31].

CO_2 tolerance must be evaluated through accelerated ageing tests due to Ba basicity and some gas impurities could affect the performance of the material under operating conditions. The accelerated ageing test of BCZP powders was performed by using TG under 10% CO_2/Ar, between room temperature and 1000 °C, with a heating/cooling rate of 5 °Cmin^{-1}.

Linear expansion coefficient of dense BCZP pellets was determined by dilatometry, between room temperature and 900 °C, under atmospheric air by using a heating/cooling rate of 1 °Cmin^{-1}. The measurements were performed by using LINSEIS L75VS1000C vertical dilatometer.

The total electrical conductivity measurements were performed by the Two Probe Method (TPM) using an Agilent 3497A multimeter. The evolution of conductivity with temperature was studied using a square bar geometry and a heating/cooling rate of 1 °Cmin^{-1} under air. The total electrical conductivity of the BCZP bar was measured between room temperature and 900 °C under (i) dry synthetic air (20% O_2/N_2), (ii) synthetic air with water vapor (~ 2% H_2O), and (iii) synthetic air with heavy water vapor (~ 2% D_2O). In addition, transport mechanisms were evaluated by Electrochemical Impedance Spectroscopy (EIS) on disc samples. Measurements were performed by using an Autolab PGSTAT30 potentiostat/galvanostat from 1 MHz to 0.1 Hz with 50 mV amplitude between 100 and 600 ºC under same conditions (i.e., dry air, wet air with water vapor, and wet air with heavy water vapor). The spectra were fitted with Equivalent Electrical Circuits (EEC), by using Zview2 software considering electrical resistance in parallel with a constant phase element (R//CPE). The dense bars and discs were painted on both sides with Pt ink.

Results And Discussion

Figure 1 shows the diffraction pattern of BCZP powder under atmospheric air at room temperature. The X-Ray data shows a single phase and it was indexed in the rhombohedral symmetry, *R-3c* space group, in agreement with previous works on barium cerates and zirconates with Pr content [32–34]. Wyckoff positions for Ba, (Ce,Zr,Pr) and O were assigned as 6a, 6b and 18e, respectively. From Rietveld method, the calculated lattice parameters (a, b, c) were: a = b = 6.087(1) Å and c = 14.958(1) Å. The angles (α, β, γ) were considered as α = β = 90 º and γ = 120 °. Also, the microstructural parameters such as average crystallite size (CS) and isotropic strains (IS) were calculated from the XRD pattern refinement, being 317(1) nm and 40.0(1) %%, respectively. Heras-Juaristi *et al.* and Antunes *et al.* indicate that low Pr-content on barium cerates and zirconates increases the phase transition temperature, and high Pr content induces several phase transitions to lower symmetry structures (*Pnma*, *Imma*, etc.) [32–34]. The TEM characterization of BCZP powder is complementary to XRD. Figure 2a displays a low-resolution image with an overall particle size of ~ 1 μm. Figures 2b and 2c show a high resolution TEM image and the Selected Area Electron Diffraction (SAED) pattern, respectively. The TEM interplanar distances are consistent with the assumption of a rhombohedral symmetry corresponding to the *R-3c* space group. Figure 2d presents the microstructure of a sintered pellet of BCZP where it can be observed a micrometric grain size ranging from ~ 2-5 μm and some degree of surface porosity, with pores of ~ 2 μm. A density of 6.02 gcm^{-3} was determined by Archimedes method, which corresponds to ~ 95 % of the theoretical density (6.36 gcm^{-3} by XRD). Similar compositions such as $Ba(Ce,Zr,Y,Pr)O_{3-\delta}$ [35], $Ba(Ce,Zr,Gd,Pr)O_{3-\delta}$ [36] and $Ba(Ce,Y,Pr)O_{3-\delta}$ [37] were also synthetized by SSR and sintered between 1400 and 1650 ºC with relative densities higher than 90 % (i.e., porosities < 10 %). The good sintering capability of these compounds is related with Pr-content in the structure.

MIEC properties (oxygen non-stoichiometry, hydration degree of oxygen vacancies, electronic charge carriers, etc.) and the operating temperature determine the different energy application perspectives for this material. It is desirable that oxygen vacancies are saturated by water vapor to improve protonic conductivity allowing to decrease operating temperatures of the electrochemical devices. Therefore, the hydration process of oxygen vacancies and its reversibility for BCZP was studied by TG. Figure 3a compares mass change of BCZP wet powder, under atmospheric air (with moist), between room temperature and 900 °C. During the heating rate, a slight increase of mass between 100 and 200 °C could be associated to water uptake from atmospheric air. A similar compound, $BaCe_{0.8}Pr_{0.2}O_{3-\delta}$ perovskite, did not evidence a mass variation under oxidizing atmosphere [21,24]. In this sense, the TG plot shows a structural water loss above 300 ºC. Also, there is not a significant mass variation between 600 and 950 ºC which indicates that the oxygen content remains almost constant and no cation reduction occurs due to oxygen loss [38]. It was assumed a negligible CO_2 adsorption/desorption and/or $BaCO_3$ formation during thermal cycling, due to the high carbonation resistance of this material (see CO_2 tolerance test, Figure 7). In addition, a hysteresis process was observed between the heating and cooling cycle. Lyagaeva *et al.* observed the same trend studying the hydration/dehydration process of $Ba(Ce,Zr,Y)O_{3-\delta}$ proton conductors by TG under air. These authors associated differences on heating and cooling cycles

to kinetic processes [39]. A DSC study was performed to detect at which temperature the water is lost. During the heating run, a broad endothermic peak appears centered at ~ 320 ºC (see Figure 3b). Although, Ohzeki *et al.* reported a reversible 2nd order phase transition of *R-3c* to *Pm-3m* at 895 ºC for $BaCeO_{3-\delta}$ [40], this is discarded due to the fact that the phase transition of BCZP occurs close to 550 °C (see phase transition, Figure 4). Moreover, we observed the same response at 280 ºC for the perovskite $Ba_{0.5}Sr_{0.5}Fe_{0.8}Cu_{0.2}O_{3-\delta}$ [38] due to water and CO_2 loss. According to these results, the endothermic peak at 320 ºC corresponds to structural water loss instead of a 2nd order phase transition. Moreover, the temperature region of weight loss in the TG measurement agrees well with the DSC result.

Previous results demonstrated that the loss or incorporation of interstitial protons into the crystal structure cause distortions of lattice parameters and ionic conductivity [31]. BCZP was studied by HT-XRD under dry synthetic air to determine if such distortions are present in this compound. A phase transition *R-3c* to *Pm-3m* occurs between 550 and 575 °C (see Figure 4a), in agreement with phase transitions detected between 400 and 600 ºC in similar compounds [32–34]. Figure 4b shows the variation of the pseudocubic lattice parameter with temperature during the heating run. A subtle slope change indicates a 2nd order phase transition between 400 and 600 °C. There is no difference between the cooling or heating behavior for the lattice parameters as a function of temperature. The lattice distortions by water incorporation/loss could not be resolved due to the low oxygen non-stoichiometry and degree of hydration. However, TG and DCS confirmed the proton incorporation on BCZP.

Figure 5 displays the linear expansion ($\Delta L/L_0$) of the BCZP sintered pellet between room temperature and 950 °C, under atmospheric air (ΔL is the length change and L_0 the initial length at 20 °C). A slight slope change was identified, between 400 and 600 °C, which shows the same trend observed by HT-XRD. TEC value obtained by dilatometry is 10.5(1) x 10^{-6} K^{-1} in agreement with the calculated by HT-XRD 11.0(1) x 10^{-6} K^{-1}. The slope change is so subtle (see inset in Figure 5) that the phase transition would not compromise the mechanical stability of the material. The TEC values for BCZP under O_2-containig atmospheres are comparable with other proton conductor electrolytes such as $Ba(Ce,Zr,Sm,Gd,Yb,Y)O_{3-\delta}$ (~ 10 x 10^{-6} K^{-1}) [41,42] which ensures good thermomechanical stability of cathode/electrolyte interface, even though thermochemical compatibility would need further testing.

Electric charge transport of MIEC materials for PC-SOFC is given by hopping of interstitial protons between oxygen sites [7] and the electronic transport associated to small polaron conductivity [43]. High electronic and protonic conductivities are necessary in order to improve ORR and proton diffusion. The total electrical conductivity measured by TPM should be a representative of the MIEC conductivity. To clarify this point, we used TPM instead of Four Probe Method due to the high resistance values of BCZP bar and negligible errors during the measurements. Otherwise, EIS technique should discriminate the transport mechanisms of the material. Therefore, TPM and EIS techniques give us complementary information. Figure 6a shows the Arrhenius plots of total conductivity by TPM under air flow. For example, the total conductivity values are 250, 64, 5 and 0.09 µS/cm at 800, 600, 400 and 200 ºC, respectively. Also, this plot shows three different zones independently of the water content and hydrogen

isotope (H/D). The change in the activation energies from one zone to other suggests a change in the transport mechanism. Below 300 ºC when H_2O is incorporated into the structure, the conductivities have a high ionic transport component (possibly mixed protonic-oxygen vacancy conductivity), whereas, once sample is dehydrated above 600 ºC, an electron-hole transport mechanism would be dominant. However, between 400 and 600 ºC the conductivity is apparently affected by the 2nd order phase transition. The ionic dominating nature of conductivity at low temperature is evidenced by EIS, showing a capacitive component typical of ionic diffusive process (see Figure 6b). To assure that conductivity measurements using low heating rates were near-equilibrium condition, different tests were performed at fixed temperatures between room temperature and 800 °C and in all cases conductivity values remain similar to the ones acquired during heating/cooling. Although previous experiments (see Figure 3) indicate water incorporation into the structure, the electrical measurements are not sensible enough to distinguish changes by change in water content and H/D nature, mainly since the high electronic conductivity with respect to ionic conductivity prevents the observation of these changes on the whole temperature range. Also, no significant differences were observed between impedance spectra under dry, H_2O and D_2O vapor atmospheres. Nevertheless, high frequency arcs present capacitance values ~ 2 pF/cm, which are associated with bulk ionic transport (b) [44]. Medium and low frequency arcs related to grain boundaries (gb) and ORR, respectively, were not detected during measurements in the whole temperature range. The bulk frequency values increase with temperature, and the arcs are no longer observed by EIS at T > 300 °C. Conductivity values between 400 and 600 °C can be extrapolated from lower temperature values (T < 200 °C), where impedance arcs are clearly observed. Similar behaviors were observed for $BaCe_{0.9}Tb_{0.1}O_{3-\delta}$ [44] and $Ba(Ce,Pr)O_{3-\delta}$ [21,24] perovskites under air. Magrasó *et al.* proposed that Pr-doping produces mixed conductor materials, where electrons and electron-holes are the minority charge carriers and defects concentration is dominated at low temperature by protons and at high temperature by oxygen vacancies [26]. These authors suggest that electron-hole conductivity prevails at high pO_2, proton conductivity becomes more significant at low temperature, low pO_2 and wet conditions, whereas the *n-type* conductivity is significant at low pO_2 and high temperatures [26]. Fabbri *et al.* calculated the transport numbers for Ba(Zr,Pr,Y) compounds from electrical conductivity measurements as a function of temperature and wet pO_2. [45]. These authors indicate that these perovskite presents mixed conductivity between 500 and 700 ºC. However, Heras-Juaristi *et al.* studied $Ba(Ce,Zr,Pr,Y)O_{3-\delta}$ perovskites by EIS and observed no difference in the electrical conductivity between wet and dry air for low Pr content sample (x = 0.2), due to the dominating character of the electron–hole component at such high oxygen activities [32]. These authors suggested that at high pO_2, electron–hole (*p-type*) conductivity is higher with respect to protonic (see Equation 1). On the other hand, water incorporation would be significant with respect to electron-hole formation at low pO_2 (see Equation 2). Although oxygen vacancies are consumed in both cases, Equation 1 indicates oxygen sites production, meanwhile Equation 2 indicates sites consumption.

$$V_O^{\bullet\bullet} + \frac{1}{2}O_{2(g)} \rightleftharpoons O_O^x + 2h^{\bullet} \quad (1)$$

$$V_O^{\bullet\bullet} + H_2O_{(g)} + O_O^x \rightleftharpoons 2OH_O^{\bullet} \quad (2)$$

Activation energy (E_a) calculated from EIS data is 0.51(1) eV, the same value obtained by TPM between 100 and 300 ºC (see Figure 6a and c). This E_a is comparable to the values for proton transport mechanism, but also to activation energies reported for other MIEC compositions with Pr as $Ba(Zr_{0.7}Ce_{0.2})_{0.8}Pr_{0.2}Y_{0.1}O_{3-\delta}$ [32] and $Ba(Ce,Pr)O_{3-\delta}$ [21,24]. Besides, the electrical conductivity values are too low as compared to these materials (~ 2 µS/cm at 200 ºC) [21,24,32], but they are comparable to the values obtained for $BaZr_{0.8}Pr_{0.2}O_{3-\delta}$ [43]. Then, all evidences confirm that BCZP presents mixed ionic and electronic conductivity. The low electrical conductivity does not fulfill the requirements for its application as PC-SOFC single phase cathode, although it would be enough as support in a composite electrode or gas separation membranes.

CO_2 tolerance must be guaranteed under specified operating conditions. Therefore, ageing tests were carried out under harsh temperature and CO_2 concentrations in order to estimate the material stability under SOFC operating condition. Figure 7a shows the weight change with temperature for BCZP powder between room temperature and 950 °C under 10 % CO_2/Ar, where no significant weight change is observed. The high stability was confirmed by XRD post CO_2 thermal treatment, where no secondary phases were detected (see Figure 7b). In the same way, Antunes *et al.* studied the CO_2 tolerance for $Ba(Zr,Pr,Y)O_{3-\delta}$ compounds, where a good tolerance was found only for very high Zr content [23]. In opposition, for Zr free compounds, significant carbonate formation is usually detected such as in other alkaline earth perovskites, e.g. $Ba_{0.5}Sr_{0.5}Co_{0.8}Fe_{0.2}O_{3-\delta}$ [46] or $BaCe_{0.8}Pr_{0.2}O_{3-\delta}$ [21,24] powders under CO_2-containing atmospheres.

Conclusion

$BaCe_{0.4}Zr_{0.4}Pr_{0.2}O_{3-\delta}$ (BCZP) perovskite was explored as a mixed ionic and electronic conductor material. At room temperature, BCZP presents rhombohedral structure, which transforms reversibly to cubic symmetry at 550 °C in dry air. Also, there is a good agreement between HT-XRD and dilatometric data, i.e., TEC $\approx 11 \times 10^{-6}\ K^{-1}$ and the 2nd order phase transition at 550 °C. TG and DSC data indicated the incorporation of a small amount of water into the structure below 300 °C. Chemical stability under CO_2-rich atmosphere was confirmed by TG.

The electrical conductivity was studied by TPM and EIS under dry and wet air, with water vapor (~ 2% H_2O) and heavy water vapor (~ 2% D_2O). Impedance spectra above 200 °C suggest mixed ionic bulk and electronic transport conduction. A transition in total conductivity was observed between 400 and 600 °C. According to this set of measurements, BCZP would present ionic conductivity below 300 ºC. BCZP low conductivity limits its applications as single phase PC-SOFC cathode. However, its high stability at PC-

SOFC operating temperatures, good thermomechanical compatibility with electrolytes and excellent CO_2 tolerance indicate that this compound could be used as oxide backbone for composite or impregnated electrodes, buffer layer, gas separation co-ionic membranes or another electrochemical application.

Declarations

Acknowledgements

This work was supported by Departamento Caracterización de Materiales (DCM), Instituto de Nanociencia y Nanotecnología (INN), Centro Atómico Bariloche-Comisión Nacional de Energía Atómica (CAB-CNEA), Consejo Nacional de Investigaciones Científicas y Técnicas (CONICET), Universidad Nacional de Cuyo (UNCu), Universidad Nacional del Sur (UNS) and Agencia Nacional de Promoción de Ciencia y Tecnología (ANPCyT). We thank to A. Baruj and B. Pentke for SEM microscopy and N. Bonanos for the discussion of the results on this work.

References

[1] Kim J, Sengodan S, Kim S, Kwon O, Bu Y, Kim G, *et al*. Proton conducting oxides: A review of materials and applications for renewable energy conversion and storage. *Renew Sustain Energy Rev* 2019, **109**: 606–618.

[2] Colomban P. Proton conductors and their applications: A tentative historical overview of the early researches. *Solid State Ionics* 2019, **334**: 125–144.

[3] Medvedev D, Trends in research and development of protonic ceramic electrolysis cells. *Int J Hydrogen Energy* 2019, **44**: 26711–26740.

[4] Rashid NLRM, Samat AA, Jais AA, Somalu MR, Muchtar A., Baharuddin NA, Wan Isahak WNR, *et al*. Review on zirconate-cerate-based electrolytes for proton-conducting solid oxide fuel cell. *Ceram Int* 2019, **45**: 6605–6615.

[5] Fabbri E, Pergolesi D, Traversa E, *et al*. Materials challenges toward proton-conducting oxide fuel cells: a critical review. *Chem Soc Rev* 2010, **39**: 4355-4369.

[6] da Silva FS, de Souza TM, *et al*. Novel materials for solid oxide fuel cell technologies: A literature review. *Int J Hydrogen Energy* 2017, **42**: 26020–26036.

[7] Kreuer KD, Proton conducting oxides. *Annu Rev Mater Res* 2003, **33**: (2003) 333–359.

[8] Norby T. Solid-state protonic conductors: principles, properties, progress and prospects. *Solid State Ionics* 1999, **125**: 1–11.

[9] Peng R, Wu T, Liu W, Liu X, Meng G, *et al*. Cathode processes and materials for solid oxide fuel cells with proton conductors as electrolytes, J Mater Chem2010, **20**: 6218-6225.

[10] Loureiro FJA, Nasani N, Reddy GS, Munirathnam NR, Fagg DP, *et al*. A review on sintering technology of proton conducting $BaCeO_3$-$BaZrO_3$ perovskite oxide materials for Protonic Ceramic Fuel Cells. *J Power Sources* 2019, **438**: 226991.

[11] Zhang C, Zhao H, *et al*. A novel cobalt-free cathode material for proton-conducting solid oxide fuel cells. *J Mater Chem* 2012, **22**: 18387-18394

[12] Zhao L, He B, Xun Z, Wang H, Peng R, Meng G, Liu X, *et al*. Characterization and evaluation of $NdBaCo_2O_{5+\delta}$ cathode for proton-conducting solid oxide fuel cells. *Int. J Hydrogen Energy* 2010, **35**: 753–756.

[13] Zhao L, He B, Ling Y, Xun Z, Peng R, Meng G, Liu X, *et al*. Cobalt-free oxide $Ba_{0.5}Sr_{0.5}Fe_{0.8}Cu_{0.2}O_{3-\delta}$ for proton-conducting solid oxide fuel cell cathode. *Int J Hydrogen Energy* 2010, **35**: (2010) 3769–3774.

[14] Zhao L, He B, Zhang X, Peng R, Meng G, Liu X, *et al*. Electrochemical performance of novel cobalt-free oxide $Ba_{0.5}Sr_{0.5}Fe_{0.8}Cu_{0.2}O_{3-\delta}$ for solid oxide fuel cell cathode. *J Power Sources* 2010, **195**: (2010) 1859–1861.

[15] Ling Y, Yu J, Lin B, Zhang X, Zhao L, Liu X, *et al*. A cobalt-free $Sm_{0.5}Sr_{0.5}Fe_{0.8}Cu_{0.2}O_{3-\delta}$–$Ce_{0.8}Sm_{0.2}O_{2-\delta}$ composite cathode for proton-conducting solid oxide fuel cells. *J Power Sources* 2011, **196**: 2631–2634.

[16] Ling Y, Zhao L, Lin B, Dong Y, Zhang X, Meng G, Liu X, *et al*. Investigation of cobalt-free cathode material $Sm_{0.5}Sr_{0.5}Fe_{0.8}Cu_{0.2}O_{3-\delta}$ for intermediate temperature solid oxide fuel cell. *Int J Hydrogen Energy* 2010, **35**: 6905–6910.

[17] Kyriakou V, Garagounis I, Vourros A, Marnellos GE, Stoukides M, *et al.* A protonic ceramic membrane reactor for the production of hydrogen from coal steam gasification. *J Memb Sci* 2018, **553**: (2018) 163–170.

[18] Chen Y, Liu H, Zhuang L, Wei Y, Wang H, *et al*. Hydrogen permeability through $Nd_{5.5}W_{0.35}Mo_{0.5}Nb_{0.15}O_{11.25-\delta}$ mixed protonic-electronic conducting membrane. *J Memb Sci* 2019, **579**: 33–39.

[19] Morejudo SH, Zanón R, Escolástico S, Yuste-Tirados I, Malerød-Fjeld H, Vestre PK, Coors WG, Martínez A, Norby T, Serra JM, Kjølseth C, *et al*. Direct conversion of methane to aromatics in a catalytic co-ionic membrane reactor. *Science* 2016, **353**: 563–566.

[20] Kalyakin AS, Lyagaeva JG, Chuikin AY, Volkov AN, Medvedev DA, *et al*. A high-temperature electrochemical sensor based on $CaZr_{0.95}Sc_{0.05}O_{3-\delta}$ for humidity analysis in oxidation atmospheres. *J*

Solid State Electrochem 2019, **23**: 73–79.

[21] Basbus JF, Moreno M, Caneiro A, Mogni LV, *et al*. Effect of Pr-Doping on Structural, Electrical, Thermodynamic, and Mechanical Properties of $BaCeO_{3-\delta}$ as Proton Conductor. *J Electrochem Soc* 2014, 161: F969–F976.

[22] Mukundan R, Davies PK, Worrell WL, *et al*. Electrochemical Characterization of Mixed Conducting $Ba(Ce_{0.8-y}Pr_yGd_{0.2})O_{2.9}$ Cathodes. *J Electrochem Soc* 2001, **148**: A82–A86.

[23] Antunes I, Mather GC, Frade JR, Gracio J, Fagg DP, *et al*. Stability of $Ba(Zr,Pr,Y)O_{3-\delta}$ materials for potential application in electrochemical devices. *J Solid State Chem* 2010, **183**: 2826–2834.

[24] Basbus JF, Arce MD, Prado F, Suescun L, Caneiro A, Mogni LV, *et al*. A high temperature study on the structure, linear expansion, thermodynamic stability and electrical properties of the $BaCe_{0.8}Pr_{0.2}O_{3-\delta}$ perovskite. *J Electrochem Soc* 2016, **163**: F516-F522.

[25] Magrasó A, Frontera C, Gunnæs AE, Tarancón A, Marrero-López D, Norby T, Haugsrud R, *et al*. Structure, chemical stability and mixed proton–electron conductivity in $BaZr_{0.9-x}Pr_xGd_{0.1}O_{3-\delta}$. *J Power Sources* 2011, **196**: 9141–9147.

[26] Magrasó A, Kjølseth C, Haugsrud R, Norby T, *et al*. Influence of Pr substitution on defects, transport, and grain boundary properties of acceptor-doped $BaZrO_3$. *Int J Hydrogen Energy* 2012, **37**: (2012) 7962–7969.

[27] Kasyanova AV, Tarutina LR, Rudenko AO, Lyagaeva JG, Medvedev DA, *et al*. $Ba(Ce,Zr)O_3$-based electrodes for protonic ceramic electrochemical cells: towards highly compatible functionality and triple-conducting behavior. *Russ Chem Rev* 2020, **89**: 667–692.

[28] Rodríguez-Carvajal J. Recent advances in magnetic structure determination by neutron powder diffraction. *Phys B Condens Matter* 1993, **192**: 55–69.

[29] Caneiro A, Bavdaz P, Fouletier J, Abriata JP, *et al*. Adaptation of an Electrochemical System for Measurement and Regulation of Oxygen Partial Pressure To a Symmetrical Thermogravimetric Analysis System Developed Using a Cahn 1000 Electrobalance. *Rev Sci Instrum* 1982, **53**: 1072–1075.

[30] Caneiro A, Chandrasekaran M, *et al*. Thermoelastic martensitic transformation in β Cu-Zn-Al studied by density changes. *Scr Metall* 1988, **22**: 1797–1800.

[31] Basbus JF, Arce MD, Prado FD, Caneiro A, Mogni LV, *et al*. A high temperature study on thermodynamic, thermal expansion and electrical properties of $BaCe_{0.4}Zr_{0.4}Y_{0.2}O_{3-\delta}$ proton conductor. *J Power Sources* 2016, **329**: 262-267.

[32] Heras-Juaristi G, Amador U, Romero de Paz J, Fuentes RO, Chinelatto AL, Ritter C, Fagg DP, Pérez-Coll D, Mather GC, *et al*. Structures, Phase Fields, and Mixed Protonic–Electronic Conductivity of Ba-Deficient, Pr-Substituted $BaZr_{0.7}Ce_{0.2}Y_{0.1}O_{3-\delta}$. *Inorg Chem* 2018, **57**: 15023–15033.

[33] Heras-Juaristi G, Amador U, Fuentes RO, Chinelatto AL, Romero de Paz J, Ritter C, Fagg DP, Pérez-Coll D, Mather GC, *et al*. Thermal evolution of structures and conductivity of Pr-substituted $BaZr_{0.7}Ce_{0.2}Y_{0.1}O_{3-\delta}$: potential cathode components for protonic ceramic fuel cells. *J Mater Chem A* 2018, **6**: 5324-5334.

[34] Antunes I, Amador U, Alves A, Correia MR, Ritter C, Frade JR, Pérez-Coll D, Mather GC, Fagg DP, *et al*. Structure and Electrical-Transport Relations in $Ba(Zr,Pr)O_{3-\delta}$ Perovskites. *Inorg Chem* 2017, **56**: 9120–9131.

[35] Melnik J, Luo J, Chuang KT, Sanger AR, *et al*. Stability and Electric Conductivity of Barium Cerate Perovskites Co- Doped with Praseodymium. *Open Fuels Energy Sci J* 2008, **1**: 7–10.

[36] Gill S, Kannan R, Maffei N, Thangadurai V, *et al*. Effect of Zr substitution for Ce in $BaCe_{0.8}Gd_{0.15}Pr_{0.05}O_{3-\delta}$ on the chemical stability in CO_2 and water, and electrical conductivity. *RSC Adv* 2013, **3**: 3599-3605.

[37] Petit CTG, Tao S, *et al*. Structure and conductivity of praseodymium and yttrium co-doped barium cerates. *Solid State Sci* 2013, **17**: 115–121.

[38] Basbus JF, Prado FD, Caneiro A, Mogni LV, *et al*. A comparative study of high temperature properties of cobalt-free perovskites. *J Electroceramics* 2014, **32**: 311–318.

[39] Lyagaeva YG, Medvedev DA, Demin AK, Tsiakaras P, Reznitskikh OG, *et al*. Thermal expansion of materials in the barium cerate-zirconate system. *Phys Solid State* 2015, **57**: 285–289.

[40] Ohzeki T, Hasegawa S, Shimizu M, Hashimoto T, *et al*. Analysis of phase transition behavior of $BaCeO_3$ with thermal analyses and high temperature X-ray diffraction. *Solid State Ionics* 2009, **180**: 1034–1039.

[41] Medvedev DA, Lyagaeva JG, Gorbova EV, Demin AK, *et al*. Progress in Materials Science Advanced materials for SOFC application: Strategies for the development of highly conductive and stable solid oxide proton electrolytes. *J Prog Mater Sci* 2016 **75**: 38–79.

[42] Medvedev D, Murashkina A, Pikalova E, Demin A, Podias A, Tsiakaras P, *et al*. $BaCeO_3$: Materials development, properties and application. *Prog Mater Sci* 2014, **60**: 72–129.

[43] Antunes I, Mikhalev S,Mather GC, Kharton VV, Figueiras FG, Alves A, Rodrigues J, Correia MR, Frade JR, Fagg DP, *et al*. Site Redistribution, Partial Frozen-in Defect Chemistry, and Electrical Properties of $Ba_{1-x}(Zr,Pr)O_{3-\delta}$. *Inorg Chem* 2016 **55**: 8552–8563.

[44] Amsif M, Marrero-López D, Ruiz-Morales JC, Savvin SN, Núñez P, *et al*. Effect of sintering aids on the conductivity of $BaCe_{0.9}Ln_{0.1}O_{3-\delta}$. *J Power Sources* 2011, **196**: 9154–9163.

[45] Fabbri E, Markus I, Bi L, Pergolesi D, Traversa E, *et al*. Tailoring mixed proton-electronic conductivity of $BaZrO_3$ by Y and Pr co-doping for cathode application in protonic SOFCs. *Solid State Ionics*2011, **202**: 30–35.

[46] Bucher E, Egger A, Caraman GB, Sitte W, *et al*. Stability of the SOFC Cathode Material (Ba,Sr)(Co,Fe)$O_{3-\delta}$ in CO_2-Containing Atmospheres. *J Electrochem Soc* 2008, **155**: B1218.

Figures

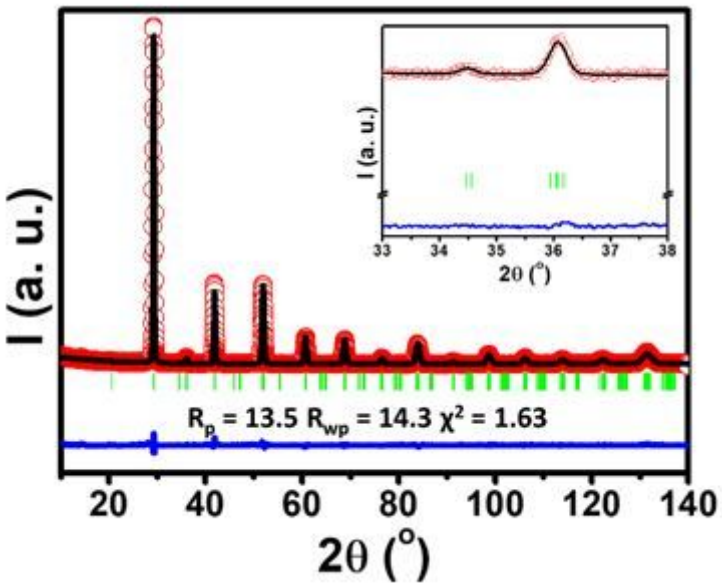

Figure 1

XRD pattern of BCZP powder under atmospheric air at room temperature, where experimental (●), calculated (–), difference between both (–) and Bragg positions (|) are indicated. The inset presents the low intensity peaks corresponding to R-3c. Goodness of fit from Rietveld Method are indicated in the figure.

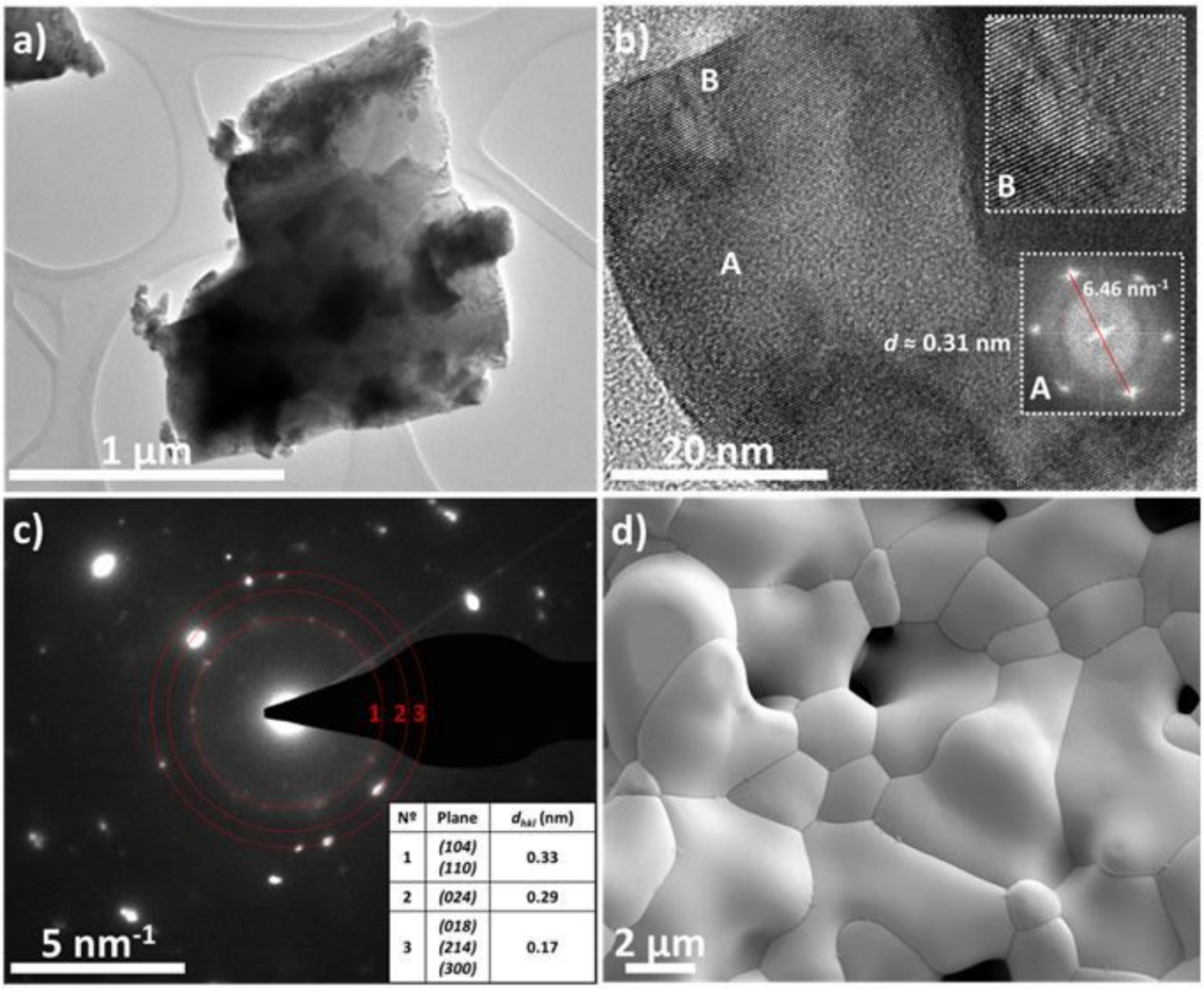

Nº	Plane	d_{hkl} (nm)
1	(104) (110)	0.33
2	(024)	0.29
3	(018) (214) (300)	0.17

Figure 2

TEM images of BCZP sample powder, a) low and b) high resolution. Fast Fourier Transform (FFT) of selected area was applied to estimate the interplanar distance d. It corresponds to (104) and (110) Miller index for R-3c. c) SAED pattern is consistent with the R-3c symmetry determined by XRD. d) SEM image of the top view of a sintered pellet presents surface porosity.

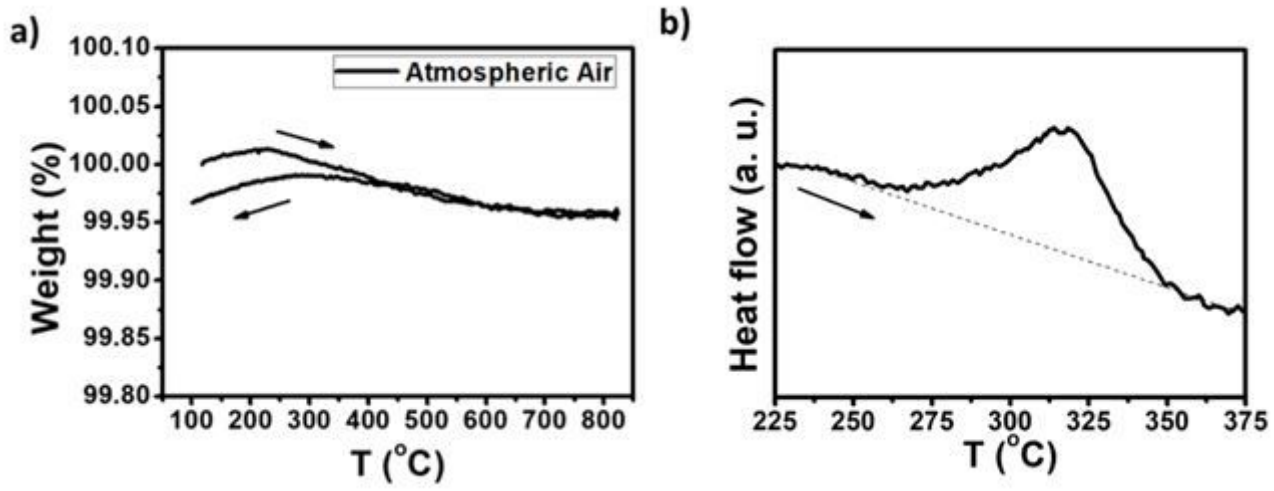

Figure 3

a) Weight (%) as a function of temperature under atmospheric air. b) DCS plot presents an endothermic peak associated to structural water loss.

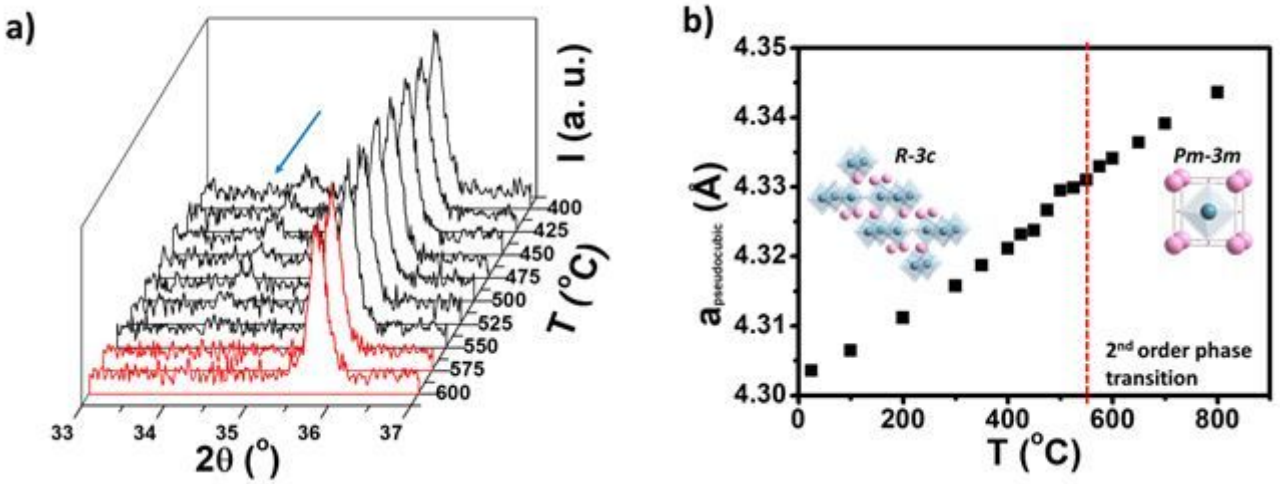

Figure 4

a) HT-XRD patterns of zoomed range under dry synthetic air. The arrow (—) indicate the evolution of low intensity peak of R-3c symmetry and red line (—) represents the phase transition to Pm-3m. b) Pseudocubic lattice parameters of BCZP powder as a function of temperature. The red dotted line represents the temperature at which the phase transition occurs.

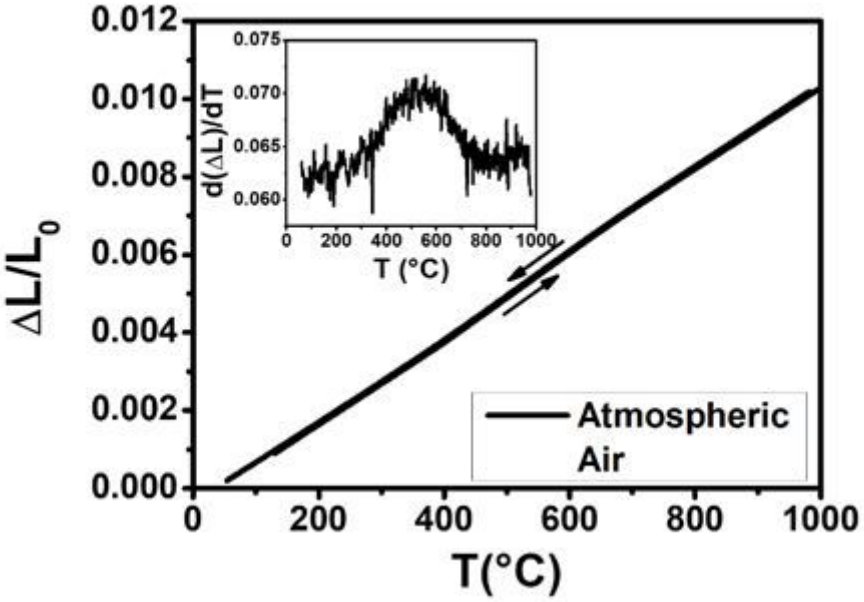

Figure 5

Linear expansion of BCZP sintered pellet as a function of temperature under atmospheric air. Inset show the derivative of the linear expansion, revealing the subtle slope change in the ΔL/L0 vs. T plot due to phase transition.

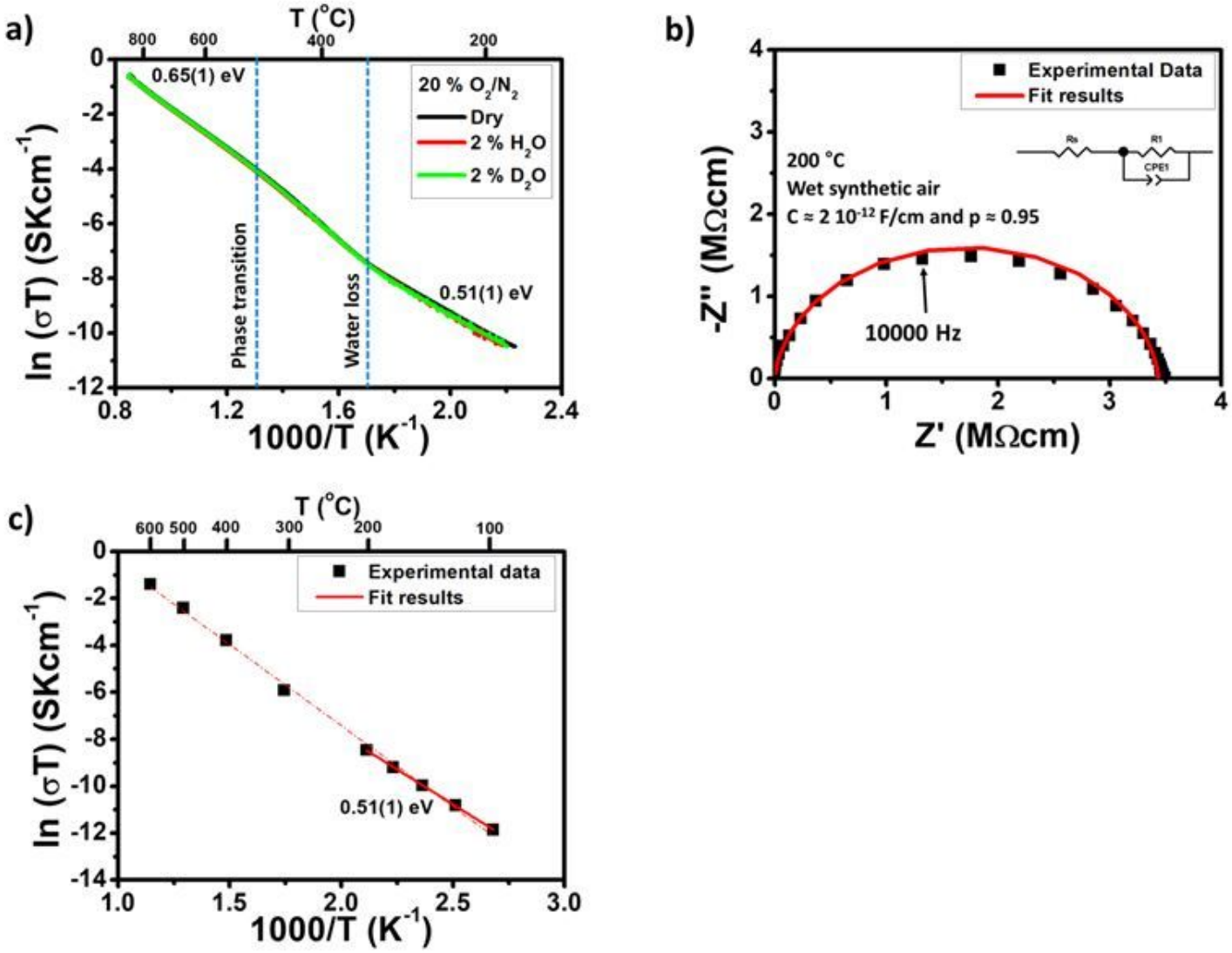

Figure 6

a) Arrhenius plots under different O2-containing atmospheres by TPM. b) Impedance Spectra collected at 200 °C and c) Arrhenius plot under wet air by EIS collected between 100 and 600 °C. Impedance spectra under dry, H2O and D2O vapor atmospheres did not show significant differences.

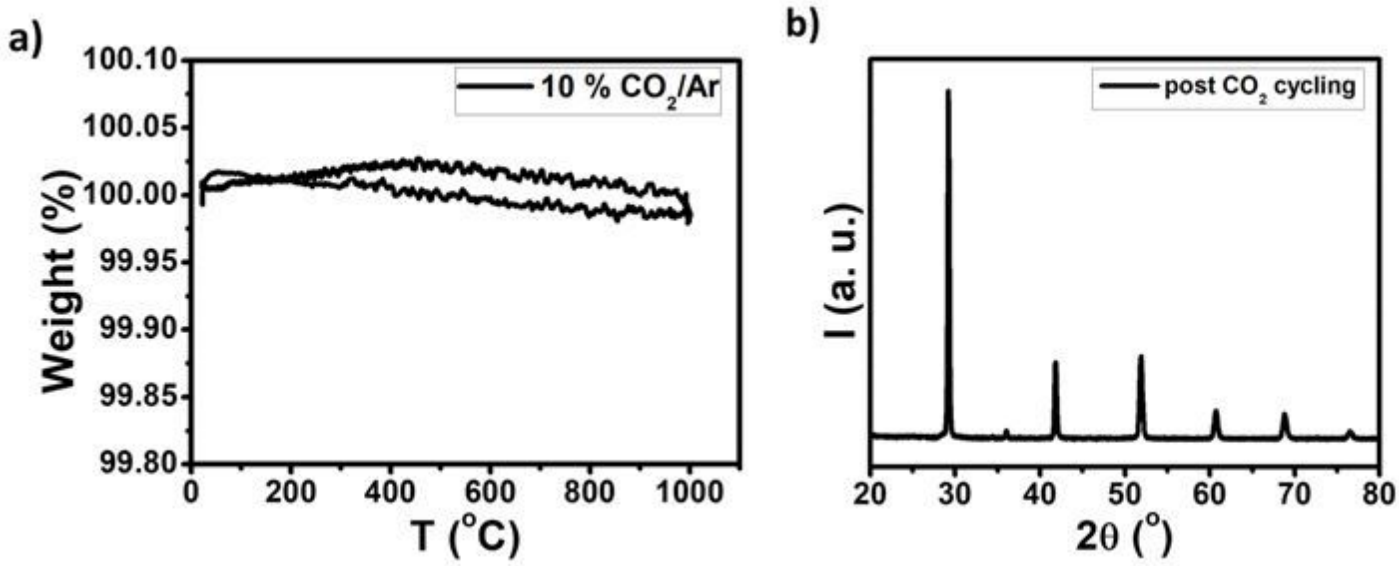

Figure 7

a) Weight (%) as function of temperature under 10 % CO2/Ar for BCZP powder. b) XRD pattern from BCZP powder after TG test, measured at room temperature in air.